nature COMMUNICATIONS

ARTICLE

Received 8 Sep 2011 | Accepted 2 Mar 2012 | Published 27 Mar 2012

DOI: 10.1038/ncomms1771

Ultra-low carrier concentration and surface-dominant transport in antimony-doped Bi_2Se_3 topological insulator nanoribbons

Seung Sae Hong[1], Judy J. Cha[2], Desheng Kong[2] & Yi Cui[2,3]

A topological insulator is the state of quantum matter possessing gapless spin-locking surface states across the bulk band gap, which has created new opportunities from novel electronics to energy conversion. However, the large concentration of bulk residual carriers has been a major challenge for revealing the property of the topological surface state by electron transport measurements. Here we report the surface-state-dominant transport in antimony-doped, zinc oxide-encapsulated Bi_2Se_3 nanoribbons with suppressed bulk electron concentration. In the nanoribbon with sub-10-nm thickness protected by a zinc oxide layer, we position the Fermi levels of the top and bottom surfaces near the Dirac point by electrostatic gating, achieving extremely low two-dimensional carrier concentration of $2\times10^{11}\,cm^{-2}$. The zinc oxide-capped, antimony-doped Bi_2Se_3 nanostructures provide an attractive materials platform to study fundamental physics in topological insulators, as well as future applications.

[1] Department of Applied Physics, Stanford University, 476 Lomita Mall, McCullough 343, Stanford, California 94305, USA. [2] Department of Materials Science and Engineering, Stanford University, 476 Lomita Mall, McCullough 343, Stanford, California 94305, USA. [3] Stanford Institute for Materials and Energy Sciences, SLAC National Accelerator Laboratory, 2575 Sand Hill Road, Menlo Park, California 94205, USA. Correspondence and requests for materials should be addressed to Y. C. (email: yicui@stanford.edu).

The exotic electronic properties of the surface state, due to its spin-momentum-locked Dirac cone in the electronic band structure, define a topological insulator as a unique class of quantum matter[1–6]. Moreover, it is predicted to offer exciting physics, such as elusive quasi-particles, spin transport and fault-tolerant quantum information processing[1–9]. Bismuth selenide (Bi_2Se_3) and its relative compounds are one of the most promising candidates to realize the ideal three-dimensional topological insulator due to their large bulk band gap and simple surface-band structure[10]. Significant advances have been made to probe the surface state in these materials by various methods, such as angle-resolved photoemission spectroscopy[11–13] and scanning-tunneling microscopy[14–16]. Transport measurements in bulk crystals have demonstrated the existence of these surface states as well[17–19].

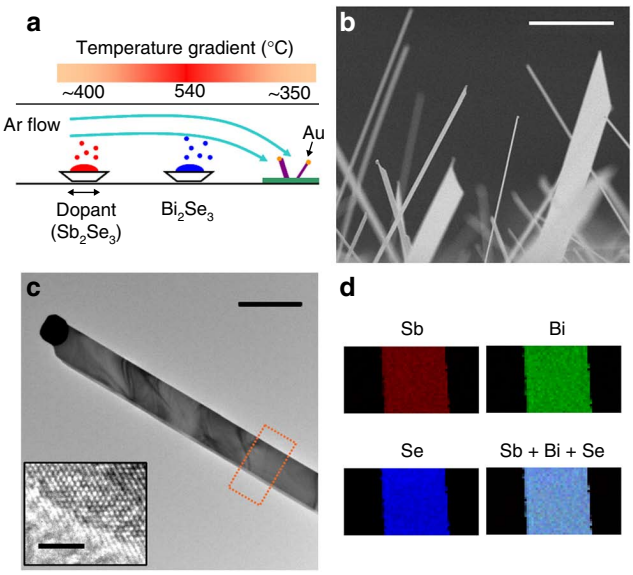

Figure 1 | Synthesis and material characterization of Sb-doped Bi_2Se_3 nanoribbons. (**a**) A schematic of vapour–liquid–solid growth of Sb-doped Bi_2Se_3 nanoribbons. By shifting the dopant source location along the temperature gradient in the tube furnace, the relative vapour pressures of two sources and the incorporated dopant level are controlled. (**b**) An scanning electron microscopy image of as-grown nanoribbons. Scale bar equals 10 μm. (**c**) A transmission electron microscopy image of a nanoribbon and its high-resolution image (inset). The rectangular box indicates the scanned area for EDX mapping. Scale bar equals 1 μm (Scale bar in the inset equals 2 nm). (**d**) Elemental maps of Sb (red), Bi (green), Se (blue) and overlaid RGB image by scanning EDX. The overlaid map looks bluish, as the Bi and Se signals are stronger than the Sb signal. The scanning map indicates homogeneous dopant distribution of 6% (atomic ratio) Sb with 0.5% s.d.

Nanoscale topological insulator devices, with their large surface-to-volume ratio, offer a unique opportunity to manifest the surface effect[20,21]. In mesoscopic length scale, transport measurements may reflect the fundamental nature of carriers, as shown in previous cases like graphene[22,23]. However, it is still challenging to study the topological surface states in the device level, as material imperfections in the bulk blur transport signatures of the surface state and limit further in-depth studies. The major challenge is the dominance of bulk carriers outnumbering surface-state carriers, mainly originating from intrinsic Se vacancies[24–27]. Moreover, the material is very sensitive to environmental contamination—several studies observed that environmental exposure (H_2O, O_2) causes material degradation and additional bulk carrier generation[17,28].

In this paper, we provide two effective solutions to eliminate both intrinsic and extrinsic sources of bulk carrier generation. First, we demonstrate vapour-phase antimony (Sb) doping in Bi_2Se_3 nanoribbons systematically suppresses the bulk conductivity. Second, we show that a zinc oxide (ZnO) capping layer on Sb-doped nanoribbons can inhibit extra carrier generation induced by extrinsic contamination. Last, in an ultrathin device with Sb doping and ZnO capping, electrostatic manipulation allows us to locate the Fermi levels of both surfaces close to the Dirac point. The effective removal of bulk carriers achieves an ideal surface-transport state that is desirable for many applications of topological insulators.

Results

Vapour-phase Sb doping and bulk carrier suppression. To suppress the bulk conductivity in topological insulator nanoribbons, we synthesize Bi_2Se_3 nanoribbons with Sb doping. Sb is known as an effective compensation dopant to reduce bulk electron density to below 10^{17} cm^{-3} in bulk crystals without destroying the topological surface state[17,29]. Bi_2Se_3 nanoribbons are synthesized via vapour–liquid–solid growth mechanism using gold particles as catalysts[20,30], and Sb vapour is introduced by the evaporation of an Antimony selenide (Sb_2Se_3) powder placed at the lower temperature zone (Fig. 1a). As-grown ribbons are typically 50–300 nm thick, 200 nm to several micrometres wide, and up to tens of micrometres long (Fig. 1b). Sb-doped Bi_2Se_3 nanoribbons are in a single crystalline rhombohedral phase (Fig. 1c), the same as undoped Bi_2Se_3 nanoribbons. The distribution of Sb dopants is spatially uniform in the nanoribbon, as confirmed by energy-dispersive X-ray spectroscopy (EDX; Fig. 1c,d). EDX spectra show simultaneous decreasing intensity of Bi peaks and increasing intensity of Sb peaks with higher Sb dopant concentrations (Supplementary Fig. S1), suggesting the doping mechanism is likely the substitution of the Bi atoms by the Sb atoms. Assuming of the substitutional doping, we calculated the Sb doping level, ranging from 0 to 7%, in atomic ratio.

The basic carrier types and densities of individual nanoribbons are measured by nanodevices with Hall bar geometry. Samples with different Sb concentrations (Table 1) all show an n-type carrier-dominant transport, as their Hall resistances are negative values. By increasing the Sb dopant concentration, the sheet resist-

Table 1 | Transport parameters of Bi_2Se_3 nanoribbon samples (not enclosed by ZnO layer) of different Sb concentrations (T=2 K, zero gate voltage).

Sample number	Sb doping (atomic %)	Sheet resistance, R_s (Ω)	Hall resistance, R_H (Ω/T)	Hall carrier density, n_H (10^{12} cm^{-2})	Thickness (nm)	ρ (mΩ cm)	μ_H ($cm^2 VS^{-1}$)
B1	0	43	−7.4	84.5	71	0.3	1,721
B2	2	177	−14.7	42.5	70	1.2	830
T1	4	422	−39.9	15.7	53	2.2	948
T2	6	975	−51	12.3	120	11.7	523
T3	7	1,350	−63.1	9.9	83	11.2	467

ance increases more than an order of magnitude and the electron density is dramatically reduced, implying the significant decrease of bulk electron contribution (Table 1). At a high Sb-doping concentration (6–7 atomic %), the carrier density is ~10^{13} cm^{-2}. Considering the electron density of the surface states from the top and bottom surfaces near the bulk conduction band edge is ~10^{13} cm^{-2} (Supplementary Fig. S2), surface carriers are now expected to have the dominant role in transport of these Sb-doped nanoribbons. As a result, the two-dimensional (2D) carrier densities of nanoribbon devices are thickness-independent when the Sb doping is close to its maximum (6–7%; Supplementary Fig. S3). The surface-dominant transport is also supported by the comparable values of the averaged carrier mobility (Hall mobility) and field-effect mobility from the surface states in low-density samples (Supplementary Table S1).

Additional electronic transport studies confirm that the bulk electron contribution is reduced significantly by the Sb doping. In Fig. 2a, temperature-dependent resistances from low Sb concentration samples (Sb 0–2%) follow typical metallic behaviour. In contrast, for the samples of high Sb concentration (Sb >4%), the resistance starts to increase and saturates at low temperature. An increase in resistance upon reducing temperature is likely due to the freeze-out of the bulk carriers. Moreover, electrostatic gating experiments in field-effect transistor devices manifest drastic difference between low and high Sb concentration samples (Fig. 2b). Low Sb-doped samples (Sb 0–2%) show weak gating dependence by a bottom gate, as the ribbon thicknesses (>70 nm) are much larger than the depletion layer thickness (~10 nm) with a relatively high carrier concentration. However, the gating response becomes larger with the increasing Sb-doping concentration. The sample with high Sb doping (T2, T3) exhibits large increase of its resistance and significant decrease in bulk carrier concentration.

The conductance of this ribbon decreases more than half by electrostatic manipulation via the bottom gate in spite of its large thickness (120 nm, T2), which strongly suggests the increase of the depletion layer depth (~35 nm) and the suppression of the bulk transport contribution. Its depletion-layer thickness can be estimated by two different ways, either by the Thomas–Fermi screening theory (for high carrier concentration) or solving the Poisson equation of charge-carrier density (for low carrier concentration). As the carrier density is low in most samples, we calculate the depletion layer thickness by solving band bending and do not consider the Thomas–Fermi screening theory. For undoped samples, the estimated depletion layer is ~10 nm, whereas for Sb-doped Bi_2Se_3 nanoribbons of low carrier concentration, it is ~35 nm, according to the approximated expression $z_d^2 = 2\kappa\varepsilon_0\Delta E/e^2 n$. In the formula, κ is the dc dielectric constant of Bi_2Se_3 (113), ΔE is the band-bending energy by gating, and n is the carrier density[24,31]. This number is based on the assumption that the carriers are distributed uniformly along the ribbon at zero gate voltage (V_g).

Magnetotransport data shows the emergence of the surface state and the suppression of bulk electrons by Sb doping. In the high-field magnetoresistance (MR), Shubnikov-de Haas (SdH) oscillations are observed in the samples of different Sb concentrations (Fig. 2c). The oscillations do not depend on the V_g, which suggests that the oscillations originate from bulk electrons (Supplementary Fig. S4). Without Sb doping, the small periodicity (B_{FFT} = 93 T) of SdH oscillations in an inverse magnetic field corresponds to the large cross-sectional area of the bulk Fermi surface in a highly metallic sample with excessive bulk carriers. As the Sb concentration increases, the oscillation period gets larger (B_{FFT} = 22 T) and disappears at high doping levels, because the bulk Fermi surface eventually becomes too small to be measured in our magnetic field range (8 T). The small cross section of the bulk Fermi surface corresponds to the decrease of the contribution of bulk electrons.

It is reasonable to ask whether the heavy Sb doping dramatically degrades bulk electron mobility, so that the oscillation disappears.

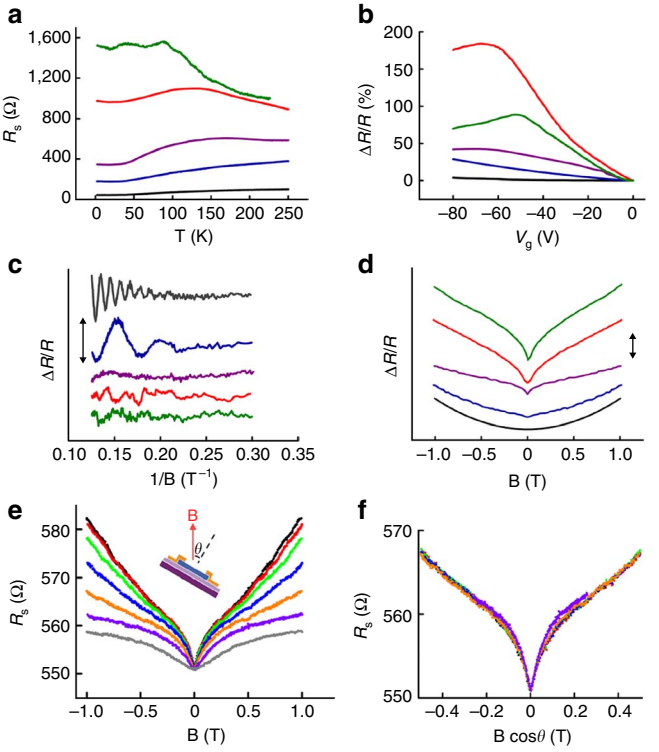

Figure 2 | Transport in nanoribbons without ZnO layer capping. (**a**–**d**) Transport measurement on nanoribbons of different doping concentration: undoped (B1, black), Sb 2% (B2, blue), Sb 4% (T1, purple), Sb 6% (T2, red), Sb 7% (T3, green). (**a**) The resistance profile versus temperature from Bi_2Se_3 nanoribbons. We note that the curves for 4 and 7% Sb doping levels are from different devices of the same growth batch. (**b**) Gating response of the resistance from Bi_2Se_3 nanoribbons (SiO_2 300-nm back gate). The resistance of high Sb concentration devices (purple, red, green) shows maximum peaks, indicating that the bottom surface switches from n-type to p-type. In general, devices of higher Sb concentrations reach the maximum peak at lower gating voltages, which suggests the Fermi level of the bottom surface to be closer to the Dirac point. (**c**) High-field MR versus inverse magnetic field (1/B). Background curve (either linear or parabolic) is subtracted from original MR curve. SdH oscillations from an undoped sample (B_{FFT}~93 T) and 2% Sb sample (B_{FFT}~22 T) correspond to bulk electron densities of ~6×10^{18} and 6×10^{17} cm^{-3}, respectively. The arrow indicates 1% magnitude of total resistance. The curves are displayed with an offset for clarity. (**d**) MR near zero magnetic field, showing clear feature of weak anti-localization from samples of high Sb concentration (Sb >3%). The arrow indicates 2% magnitude of total resistance. Each curve is normalized by zero field resistance and displayed with an offset for clarity. (**e**) Angle-dependent MR (~5% Sb-doped sample, n_H = 2×10^{13} cm^{-2}, d = 100 nm) with seven different field orientations: 0° (black), 15° (red), 30° (lime), 45° (blue), 60° (orange), 75° (purple), 90° (grey). Inset: a cartoon to describe the angle definition in the experiment. (**f**) MR with different field orientations, as a function of the perpendicular field component. All measurement are conducted at T = 2 K except temperature-dependant studies.

A previous study on bulk crystals showed strong bulk electron SdH oscillations observed from samples of heavy Sb doping, implying high electron mobility despite the large amount of dopants[17]. We also test the effect of doping on electron mobility, starting with a high Sb concentration sample (T3, without the ZnO layer initially) of low carrier concentration (10^{13} cm^{-2}). Within the 8 T range, we could not see any oscillatory features comparable to the SdH oscillations. Then, we put the ZnO layer (~10 nm) to protect

the device from environmental doping during heating, and the sample was heat-treated at 100 °C for 4 h in moderate vacuum (~1 Torr argon gas-filled chamber). After the heat treatment, carrier concentration increased a lot (2.5×10^{13} cm^{-2}) and the SdH oscillations (B_{FFT} = 17 T, E_F = 16 meV above the conduction band edge) emerged (Supplementary Fig. S4). A temperature of 100 °C may not be regarded as a high-enough temperature to improve crystal quality, as we observed large carrier density increase from other samples, presumably by creating more Se vacancies. In this device, we also confirm that the Hall carrier density increases substantially. Therefore, we conclude that the electron mobility does not degrade by doping, and the fading of SdH oscillations is because of the elimination of bulk electrons.

Weak anti-localization (WAL), the quantum correction in the spin-orbit-coupled surface state[25,32], is absent in the MR trace of the undoped sample (Fig. 2d, B1), as the large bulk electron contribution masks the surface-state transport. Samples with higher Sb concentration (Fig. 2d, T1, T2, T3), in contrast, manifest the characteristic WAL as the sharp cusp near zero magnetic field due to the suppression of bulk conductivity. We conduct an angle-dependent study to verify the dominance of the 2D component in WAL; MR of a nanoribbon (Sb~5%) was measured at different field orientations (Fig. 2e). The cusp is the sharpest with the magnetic field perpendicular to the basal plane and becomes flatter as the angle (θ) increases. When the MR from different field orientations are plotted as a function of the perpendicular field ($B\cos\theta$; Fig. 2f), they overlay nicely with the 0° MR, implying the observed WAL is essentially controlled by the 2D component. Additional fitting procedures are discussed in the Supplementary information (Supplementary Fig. S5, Supplementary Methods).

ZnO protective layer. So far, we have shown that Sb doping effectively reduces bulk carriers. However, nanoribbons are still exposed to extrinsic contaminations during device fabrication, which can increase the bulk carrier concentration as well[17,28]. Therefore, we hypothesize that the intrinsic carrier density of the Sb-doped Bi_2Se_3 should be much lower than that measured, and a protection layer is needed to access the intrinsic carrier density. We use ZnO for the protective layer due to the insulating properties of intrinsic ZnO, and its chemical stability against moisture and standard solvents in a wide range of temperature. Also, it can be deposited by a sputtering process without elevation of substrate temperature, avoiding additional Se vacancies generation upon heating. The sputtered ZnO layer covers the entire surface of the nanoribbons, which prevents degradation and extrinsic doping associated with the standard fabrication process. We compare carrier densities of 20 samples (10 with ZnO, 10 without ZnO capping) of different Sb concentrations (Supplementary Fig. S6). On average, the ZnO-capped samples exhibit lower carrier densities than uncapped devices of similar Sb concentrations. Also, ZnO capping improves both the Hall mobility and the field-effect mobility. For samples of high Sb concentration (Sb = 6–7%), the average Hall mobility of uncapped devices is ~500 (cm^2 V^{-1}s^{-1}), whereas the average Hall mobility of ZnO-protected devices is ~750 (cm^2 V^{-1}s^{-1}).

In a bottom-gate device (Fig. 3a) fabricated on an Sb-doped, ZnO-protected nanoribbon of 200 nm in thickness, the carrier density is very low (~5×10^{12} cm^{-2}), and the gate-dependent resistance shows that the Fermi level of the bottom surface is close to the Dirac point even without applying the V_g (Table 2). In Fig. 3b, its resistance decreases by either direction of the gating voltage, and the Hall resistance increases due to the electrostatic accumulation of charge carriers at the bottom surface (p-type carriers for negative V_g and n-type carriers for positive V_g).

The gate-dependent temperature curve study also confirms that the Fermi level of the bottom surface is close to the Dirac point. The temperature-dependent resistance shows a non-metallic behaviour

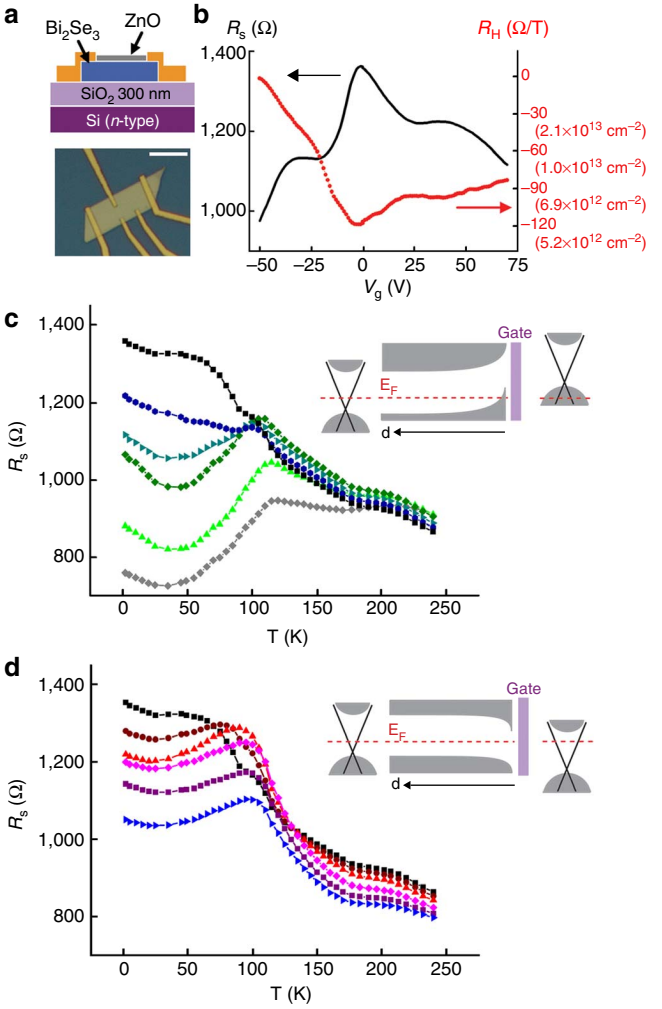

Figure 3 | Transport in a thick Sb-doped Bi_2Se_3 nanoribbon with ZnO layer. (**a**) Device (Z1) schematic (top) and optical image (bottom) of a thick sample (200 nm) of Sb 7% concentration. Scale bar equals 5 μm. (**b**) Gate-voltage dependence of longitudinal sheet resistance (R_S) and Hall resistance (R_H) measured at low field (B < 2 T) at T = 2 K. Hall resistance increases in both direction of V_g, implying that the Fermi level of the bottom surface is near the Dirac point at zero gating voltage. The anomalous kink in the longitudinal resistance curve is not well understood, and it is not reproducible in other samples. (**c**) Temperature-dependent resistance curve at different V_g (negative): 0 V (black), −10 V (blue), −20 V (teal), −40 V (green), −60 V (lime), −80 V (grey). The curve changes significantly as more bulk holes are added, reflecting the conventional metallic temperature dependence of induced carriers. A band diagram (inset) shows band bending at the bottom surface induced by gating. (**d**) Temperature-dependent resistance curve at different V_g (positive): 0 V (black), +10 V (maroon), +20 V (red), +40 V (pink), +60 V (purple), +80 V (blue). In a band diagram (inset), the Fermi level does not cross any bulk band by positive gating, explaining the qualitatively similar temperature curves over the wide range of gating voltage.

at zero V_g, with the increase of resistance by lowering the temperature, and saturating at low temperature. By introducing holes with the negative V_g (Fig. 3c), resistance starts to drop down by cooling (T < 120 K), indicating the generation of bulk carriers, whereas the general behaviour does not change by inducing more electrons (positive V_g, Fig. 3d). The asymmetric temperature-dependent transport by different gating reflects the characteristic band structure near the Dirac point of Bi_2Se_3. From the angle-resolved photoemission

Table 2 | Transport parameters of Bi_2Se_3 nanoribbon samples enclosed by ZnO layer (T=2 K, zero gate voltage)

Sample number	Sb doping (atomic %)	Sheet resistance, R_s (Ω)	Hall resistance, R_H (Ω/T)	Hall carrier density, n_H (10^{12} cm^{-2})	Thickness (nm)	ρ (mΩ cm)	μ_H (cm^2 V^{-1}s^{-1})
Z1	7	1,350	−122	5.1	200	27	903
Z2	5	4,760	−280	2.8	6	2.9	470

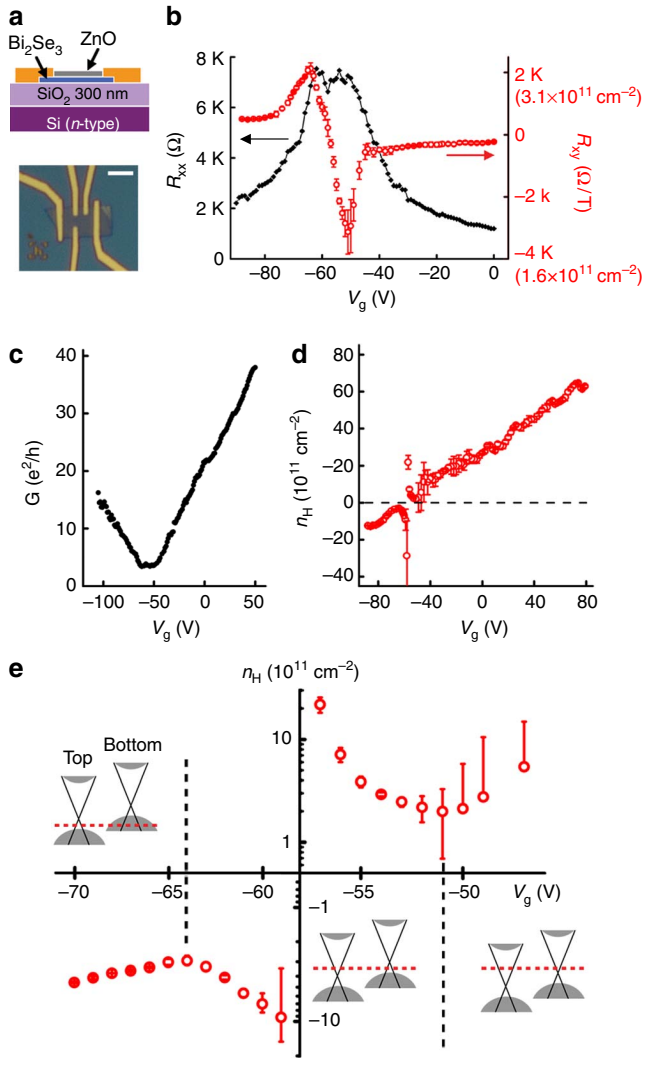

Figure 4 | Transport in an ultrathin Sb-doped Bi_2Se_3 nanoribbon with ZnO layer. (**a**) Device (Z2) schematic (top) and optical image (bottom) of thin ribbon sample (6 nm) of Sb 5% concentration. Scale bar indicates 3 μm. (**b**) V_g dependence of longitudinal resistance (R_{xx}) and Hall resistance (R_{xy}) measured at low magnetic field (B<1 T), at T = 2 K. Hall resistance decreases as n-type carriers are depleted (V_g > −50 V); increases as induced p-type carriers from the bottom surface form a mixed state with decreasing n-type carriers (−65 V < V_g < −50 V); and decreases again as the entire sample becomes a hole conductor (V_g < −65 V). (**c**) Conductance (G) versus V_g curve is linear, except near the minimum conductance (equivalent to the conductivity of 0.9 G_0). (**d**) Electron density (n_H) plot as a function of V_g. It depends on V_g linearly in the wide range of voltage (−90 V to +80 V). (**e**) Semi-log scale plot of carrier density near its charge neutrality point (Dirac point). Band diagrams of top and bottom surfaces (inset) for samples with pure p-type conduction (left), mixed conduction (middle) and pure n-type conduction (right).

spectroscopy studies[11,32], the Dirac point of surface states is just above the bulk valence-band edge and far apart from the bulk conduction band edge (~0.2 eV). Within the range of V_g (+80 V), positive gating only accumulates more electrons from the bottom surface band of the thick nanoribbon (inset of Fig. 3d), which does not change the overall shape of the temperature curve. In contrast, bulk electronic states are easily populated from the valence band by negative gating (inset of Fig. 3c), and the ribbon is in a mixed state with the coexistence of electrons and holes (Supplementary Fig. S7). This temperature-dependent study confirms the independent tuning of the Fermi level of one surface near the Dirac point. Such a material system may allow the creation of a topological insulator junction of both types of carriers or a single surface junction to study novel proximity effects in the future[8,9].

Electrostatic manipulation of the Fermi level in an ultrathin device. In addition to the manipulation of the bottom surface in the thick ribbons by substrate gating, the most attractive step is the flexible manipulation of the Fermi levels of both top and bottom surfaces, to position them close to the Dirac point. Such a control by electrostatic gating requires the nanoribbons to be thinned down. We etched a thick, Sb-doped ribbon (~100 nm) by argon plasma in a sputtering machine, and *in situ* deposited a 15-nm thick ZnO protection layer. In Fig. 4a, the ribbon is semitransparent with a thickness of 6 nm, more than 30 times thinner than the previous device (Fig. 3). This device has a very low electron concentration of 2.8×10^{12} cm^{-2} at zero V_g (Fig. 4b), roughly four times lower than that (~10^{13} cm^{-2}) of the maximum density for pure surface conduction in the bulk band gap (Table 2). Accordingly, the Fermi levels of both the top and bottom surfaces are completely within the bulk band gap. In other words, the Fermi level crosses only the surface Dirac cone above the Dirac point.

In this ultrathin nanoribbon with very low carrier concentration, its small thickness of 6 nm makes it possible to shift the Fermi level of the entire ribbon by electrostatic gating across the Dirac point. By sweeping V_g from positive to negative bias, its longitudinal resistance (R_{xx}) initially increases and reaches a peak value (~7 kΩ) around V_g of −50 V, and then decreases when further applying negative gate bias (black curve, Fig. 4b). The corresponding Hall slope (red curve, Fig. 4b) increases by more than ten times, and then switches the sign when R_{xx} reaches the peak value. These results clearly demonstrate the ambipolar field effect and suggest that the entire sample is converted from n-type to p-type. The sample conductance depends on the gating voltage linearly, except at the plateau of minimum conductance (~3.6 G_0, equivalent to 2D conductivity of 0.9 G_0, where G_0 is e^2/h; Fig. 4c). The absence of zero conductance region during the ambipolar transition is due to the gapless surface states. The carrier density obtained by the Hall resistance, shown in Fig. 4d, also linearly depends on V_g. The sample remains purely n-type until V_g = −50 V, switches to a mixed carrier state in the range of −65 V < V_g < −50 V, and eventually to p-type when V_g < −65 V (Fig. 4e).

Discussion

In the ultrathin device, the extremely low carrier density of $n_H = 2\times10^{11}$ cm^{-2} observed at V_g of −51 V indicates the Fermi

levels of both surfaces simultaneously approach the Dirac point (Supplementary Fig. S2). The removal of bulk electrons in topological insulator nanostructures achieves this stringent condition to study interesting physics near the Dirac point by transport. For example, the dimensional crossover by the top and bottom surface hybridization creates the surface band gap at the Dirac point and may possess exotic edge states[13,33,34]. Massive Dirac Fermions[35] and a new type of Hall effect[36], by incorporation of magnetic dopants, will be another important physics near the Dirac point. Our experiment opens up the possibility that such interesting physics can be studied in nanoscale device transport, providing the material tunable near the Dirac point without excessive residual carriers. We also note that some studies propose that inhomogeneous Coulomb potential near the Dirac point[26,37] can contribute to the minimum carrier density, similar to the case of graphene[22,23]. It would be another interesting topic in topological insulator transport, and further study is expected to understand the observed minimum conductivity.

Methods

Material synthesis and device fabrication. The synthesis of Sb-doped Bi_2Se_3 nanoribbons was carried out in a 12-inch horizontal tube furnace with a quartz tube. Bi_2Se_3 source powder (99.999%) from Alfa Aesar was placed in the centre of the furnace; Sb_2Se_3 source powder (99.999%) was placed at an upstream lower temperature zone; and the growth substrate, silicon wafer with thermally-evaporated 10 nm Au film, was placed at a downstream zone. High-purity argon gas was used to convey vapour from the source materials to a growth substrate at 130-s.c.c.m flow rate. During the entire growth time of 1.5 h, 1 Torr pressure and 540 °C centre zone temperature were maintained. The Sb dopant concentration in nanoribbons can be controlled by varying the Sb_2Se_3 source powder temperature—using the temperature gradient in the tube furnace; we placed the Sb_2Se_3 source powder at different locations of the tube furnace, resulting in variation of the Sb_2Se_3 source powder temperature. The estimated temperatures of the Sb_2Se_3 source and the growth substrate are 450 and 350 °C, respectively, for the highest Sb concentration sample. After the vapour–liquid–solid growth, nanoribbons were directly transferred onto a doped silicon substrate with a 300-nm silicon dioxide layer. Then, a 15-nm thick ZnO layer was deposited by sputtering to cover the nanoribbon samples. In case of the thin ribbon sample, nanoribbons were etched by argon/metal plasma and capped by the ZnO layer *in situ*. The chemical composition and the surface roughness did not change with the Ar plasma etching, which were checked with Auger electron spectroscopy and atomic force microscopy (AFM). The nanoribbon devices were fabricated by standard e-beam lithography, and the ZnO layer on the contact area was etched by diluted base solution (tetramethyl-ammonium hydroxide) followed by thermal evaporation of Cr/Au contact (5 nm/80 nm). The samples were stored in an N2 glovebox (H_2O, $O_2 < 1$ p.p.m.) at room temperature between processes. The device is usually measured within 1 or 2 days after device fabrication and 2 to 3 days after nanoribbon synthesis.

Cryogenic transport measurement. All transport measurements (except angle-dependant transport) were carried out in an Oxford ^{4}He cryostat with superconducting magnet, using low-frequency (~200–1 kHz) AC technique by digital lock-in amplifiers (Stanford Research Systems SR830) with current-driven configuration. Angle-dependant transport measurements were carried out in a Quantum Design PPMS-7 instrument, Janis 9T magnet He-cryostats (base temperature 2 K, low-frequency 1 kHz). A DC sourcemeter (Keithley 2400) was used to apply back V_g with negligible leakage current (< 1 nA). All samples were measured in either Hall-bar geometry or four-terminal configuration. The R_{xx} curves were obtained by measuring the four-point resistance using the standard AC lock-in set-up while sweeping the V_g continuously using the DC sourcemeter. Sheet resistances (Rs), conductivities and resistivities were obtained by measuring the device dimension by AFM/scanning electron microscopy. For the gate-dependent Hall measurement, we measured the Hall voltage at five different fields ($B = -1$ T, -0.5 T, 0 T, 0.5 T, 1 T) while sweeping the gate and checked that the Hall slope is linear. The base temperature for all measurements was 2 K, except during the temperature-dependant studies.

Material characterization. For structural and elemental analysis, scanning transmission electron microscopy/transmission electron microscopy (FEI Tecnai G2 F20 X-Twin microscope, acceleration voltage 200 kV) equipped with an EDX spectrometer was used. The EDX spectra obtained from nanoribbons of different Sb concentrations are normalized to Se peaks (11.2 keV) for comparison. Typically, the EDX acquisition time was 300 s for all spectra for good signal-to-noise ratios (Supplementary Fig. S1).

Optical images were taken with Olympus BX51M and the scanning electron microscopy image was taken with FEI XL30 Sirion. AFM data were taken with Park Systems XE-70/XE-100.

References

1. Moore, J. E. The birth of topological insulators. *Nature* **464,** 194–198 (2010).
2. Qi, X.- L. & Zhang, S.- C. Topological insulators and superconductors. *Rev. Mod. Phys.* **83,** 1057–1110 (2011).
3. Hasan, M. Z. & Kane, C. L. Colloquium: topological insulators. *Rev. Mod. Phys.* **82,** 3045 (2010).
4. Fu, L. & Kane, C. Topological insulators with inversion symmetry. *Phys. Rev. B* **76,** 045302 (2007).
5. Konig, M. *et al.* Quantum spin hall insulator state in HgTe quantum wells. *Science* **318,** 766–770 (2007).
6. Hsieh, D. *et al.* A topological Dirac insulator in a quantum spin Hall phase. *Nature* **452,** 970–974 (2008).
7. Qi, X.- L., Li, R., Zang, J. & Zhang, S.- C. Inducing a magnetic monopole with topological surface states. *Science* **323,** 1184–1187 (2009).
8. Seradjeh, B., Moore, J. E. & Franz, M. Exciton condensation and charge fractionalization in a topological insulator film. *Phys. Rev. Lett.* **103,** 066402 (2009).
9. Fu, L. & Kane, C. Superconducting proximity effect and majorana fermions at the surface of a topological insulator. *Phys. Rev. Lett.* **100,** 096407 (2008).
10. Zhang, H. *et al.* Topological insulators in Bi_2Se_3, Bi_2Te_3 and Sb_2Te_3 with a single Dirac cone on the surface. *Nat. Phys.* **5,** 438–442 (2009).
11. Xia, Y. *et al.* Observation of a large-gap topological-insulator class with a single Dirac cone on the surface. *Nat. Phys.* **5,** 398–402 (2009).
12. Chen, Y. L. *et al.* Experimental realization of a three-dimensional topological insulator, Bi_2Te_3. *Science* **325,** 178–181 (2009).
13. Zhang, Y. *et al.* Crossover of the three-dimensional topological insulator Bi_2Se_3 to the two-dimensional limit. *Nat. Phys.* **6,** 584–588 (2010).
14. Roushan, P. *et al.* Topological surface states protected from backscattering by chiral spin texture. *Nature* **460,** 1106–1109 (2009).
15. Alpichshev, Z. *et al.* STM imaging of electronic waves on the surface of Bi_2Te_3: topologically protected surface states and hexagonal warping effects. *Phys. Rev. Lett.* **104,** 016401 (2010).
16. Hanaguri, T., Igarashi, K., Kawamura, M., Takagi, H. & Sasagawa, T. Momentum-resolved Landau-level spectroscopy of Dirac surface state in Bi_2Se_3. *Phys. Rev. B.* **82,** 081305 (2010).
17. Analytis, J. G. *et al.* Two-dimensional surface state in the quantum limit of a topological insulator. *Nat. Phys.* **6,** 960–964 (2010).
18. Qu, D.- X., Hor, Y. S., Xiong, J., Cava, R. J. & Ong, N. P. Quantum oscillations and hall anomaly of surface states in the topological insulator Bi_2Te_3. *Science* **329,** 821–824 (2010).
19. Taskin, A. A., Ren, Z., Sasaki, S., Segawa, K. & Ando, Y. Observation of Dirac holes and electrons in a topological insulator. *Phys. Rev. Lett.* **107,** 016801 (2011).
20. Peng, H. *et al.* Aharonov–Bohm interference in topological insulator nanoribbons. *Nat. Mater.* **9,** 225–229 (2009).
21. Xiu, F. *et al.* Manipulating surface states in topological insulator nanoribbons. *Nat. Nano.* **6,** 216–221 (2011).
22. Zhang, Y., Tan, Y.- W., Stormer, H. L. & Kim, P. Experimental observation of the quantum Hall effect and Berry's phase in graphene. *Nature* **438,** 201–204 (2005).
23. Novoselov, K. S. *et al.* Two-dimensional gas of massless Dirac fermions in graphene. *Nature*. **438,** 197–200 (2005).
24. Checkelsky, J. G., Hor, Y. S., Cava, R. J. & Ong, N. P. Bulk band gap and surface state conduction observed in voltage-tuned crystals of the topological insulator Bi_2Se_3. *Phys. Rev. Lett.* **106,** 196801 (2011).
25. Steinberg, H., Laloë, J.- B., Fatemi, V., Moodera, J. S. & Jarillo-Herrero, P. Electrically tunable surface-to-bulk coherent coupling in topological insulator thin films. *Phys. Rev. B.* **84,** 233101 (2011).
26. Kim, D. *et al.* Electronic transport in the topological insulator regime: approaching the Dirac point in Bi_2Se_3. Preprint athttp://arxiv.org/abs/1105.1410 (2011).
27. Kong, D. *et al.* Ambipolar field effect in topological insulator nanoplates of $(Bi_xSb_{1-x})_2Te_3$. by composition tuning. *Nat. Nano.* **6,** 705–709 (2011).
28. Kong, D. *et al.* Rapid surface oxidation as a source of surface degradation factor for Bi_2Se_3. *ACS Nano.* **5,** 4698–4703 (2011).
29. Zhang, Y. *et al.* Doping effects of Sb and Pb in epitaxial topological insulator Bi_2Se_3 thin films: an *in situ* angle-resolved photoemission spectroscopy study. *Appl. Phys. Lett.* **97,** 194102 (2010).
30. Kong, D. *et al.* Topological insulator nanowires and nanoribbons. *Nano. Lett.* **10,** 329–333 (2010).
31. Analytis, J. G. *et al.* Bulk Fermi surface coexistence with Dirac surface state in Bi_2Se_3: a comparison of photoemission and Shubnikov-de Haas measurements. *Phys. Rev. B.* **81,** 205407 (2010).
32. Chen, J. *et al.* Gate-voltage control of chemical potential and weak antilocalization in Bi_2Se_3. *Phys. Rev. Lett.* **105,** 176602 (2010).
33. Linder, J., Yokoyama, T. & Sudbø, A. Anomalous finite size effects on surface states in the topological insulator Bi_2Se_3. *Phys. Rev. B.* **80,** 205401 (2009).

34. Liu, C.- X. *et al.* Oscillatory crossover from two-dimensional to three-dimensional topological insulators. *Phys. Rev. B.* **81,** 041307 (2010).
35. Chen, Y. L. *et al.* Massive Dirac Fermion on the surface of a magnetically doped topological insulator. *Science* **329,** 659–662 (2010).
36. Yu, R. *et al.* Quantized anomalous Hall effect in magnetic topological insulators. *Science* **329,** 61–64 (2010).
37. Culcer, D., Hwang, E. H., Stanescu, T. D. & Das Sarma, S. Two-dimensional surface charge transport in topological insulators. *Phys. Rev. B.* **82,** 155457 (2010).

Acknowledgements

We thank K. Lai and J. R. Williams for the helpful discussions, and B. Weil for the help in the manuscript preparation. Y. C. acknowledges the supports from the Keck Foundation, DARPA MESO project (No. N66001-11-1-4105) and the King Abdullah University of Science and Technology (KAUST) Investigator Award (No. KUS-l1-001-12).

Author contributions

S.S.H. and Y.C. conceived the experiments. S.S.H. carried out synthesis and device fabrication, and J.J.C. carried out structural characterization. S.S.H., J.J.C. and D.K. carried out transport measurements and analysis. All authors contributed to writing of the manuscript.

Additional information

Supplementary Information accompanies this paper at http://www.nature.com/naturecommunications

Competing financial interests: The authors declare no competing financial interests.

Reprints and permission information is available online at http://npg.nature.com/reprintsandpermissions/

How to cite this article: Hong, S.S. *et al.* Ultra-low carrier concentration and surface-dominant transport in Sb-doped Bi_2Se_3 topological insulator nanoribbons. *Nat. Commun.* 3:757 doi: 10.1038/ncomms1771 (2012).